

This is a repository copy of *Magnetoresistance Dynamics in Superparamagnetic Co-Fe- B Nanodots*.

White Rose Research Online URL for this paper:

<https://eprints.whiterose.ac.uk/157965/>

Version: Published Version

Article:

Parks, Brad, Abdelgawad, Ahmed, Wong, Thomas et al. (2 more authors) (2020)
Magnetoresistance Dynamics in Superparamagnetic Co-Fe- B Nanodots. *Physical Review Applied*. 014063. ISSN 2331-7019

<https://doi.org/10.1103/PhysRevApplied.13.014063>

Reuse

Items deposited in White Rose Research Online are protected by copyright, with all rights reserved unless indicated otherwise. They may be downloaded and/or printed for private study, or other acts as permitted by national copyright laws. The publisher or other rights holders may allow further reproduction and re-use of the full text version. This is indicated by the licence information on the White Rose Research Online record for the item.

Takedown

If you consider content in White Rose Research Online to be in breach of UK law, please notify us by emailing eprints@whiterose.ac.uk including the URL of the record and the reason for the withdrawal request.


Magnetoresistance Dynamics in Superparamagnetic Co-Fe-B Nanodots

Brad Parks,¹ Ahmed Abdelgawad,² Thomas Wong,¹ Richard F.L. Evans,³ and Sara A. Majetich^{1,*}

¹ *Physics Department, Carnegie Mellon University, Pittsburgh, Pennsylvania 15213, USA*

² *Materials Science and Engineering Department, Carnegie Mellon University, Pittsburgh, Pennsylvania 15213, USA*

³ *Department of Physics, University of York, Heslington, York YO10 5DD, United Kingdom*

 (Received 10 October 2019; revised manuscript received 25 November 2019; published 30 January 2020)

Individual disk-shaped Co-Fe-B nanodots are driven into a superparamagnetic state by a spin-transfer torque, and their time-dependent magnetoresistance fluctuations are measured as a function of current. A thin layer of oxidation at the edges has a dramatic effect on the magnetization dynamics. A combination of experimental results and atomistic spin simulations shows that pinning to oxide grains can reduce the likelihood that fluctuations lead to reversal, and can even change the easy-axis direction. Exchange-bias loop shifts and training effects are observed even at room temperature after brief exposure to small fields. The results have implications for studies of core-shell nanoparticles and small magnetic tunnel junctions and spin-torque oscillators.

DOI: [10.1103/PhysRevApplied.13.014063](https://doi.org/10.1103/PhysRevApplied.13.014063)

I. INTRODUCTION

Superparamagnetism has been studied for many years [1–3], but is still of great interest today [4]. Superparamagnetic particles are used in many biomedical applications [5,6], mainly because the fluctuations minimize magnetically driven aggregation. Programmable superparamagnets could form the basis for a new type of probabilistic computing using magnetic tunnel junctions (MTJs) [7–10]. Superparamagnetism is also relevant to spintronic applications such as magnetic random access memory (MRAM) [11–13] and spin-torque oscillators (STOs) [14], where at small diameters stochastic fluctuations are undesirable but difficult to avoid.

Traditional superparamagnets are monodomain nanoparticles that switch between two metastable states, with an average retention time between switches that depends on the temperature and magnetic field. For spintronics, the superparamagnets are disc-shaped nanomagnets rather than ellipsoidal particles. While they need not switch by coherent rotation, the metastable ground states are still monodomain. The average fluctuation rate in traditional superparamagnets is controlled by temperature and magnetic field. When part of an electronic device, the frequency of these stochastic fluctuations may also be tuned by spin-transfer torque (STT) [14], spin-orbit torque, or voltage control of magnetic anisotropy [15]. Here we focus on Co-Fe-B superparamagnets that are most relevant for spintronics applications. These thin (2.5-nm) Co-Fe-B

nanodots 20–80 nm in diameter form the free layer of in-plane MTJs and have either parallel (P) or antiparallel (AP) magnetization relative to an unpatterned fixed layer. STT is used to drive the nanodots into a superparamagnetic state, and the magnetoresistance fluctuations are analyzed as a function of time, tunnel current, and dot diameter. Our findings show that it is possible to tune the time-averaged state from P to AP for any size, but that the average time between switching events is very sensitive to edge oxidation, which can lead to exchange-bias effects.

II. METHODS

A. Sample preparation

The superparamagnetic nanodots studied here are circular nanodots of Co-Fe-B 20–80 nm in diameter and 2.5 nm thick, separated by a 1-nm MgO tunnel barrier from the unpatterned magnetic reference layer consisting of a synthetic ferrimagnet with an antiferromagnetic Pt-Mn pinning layer.

The original film stack is grown by Everspin Technologies [16], and consists of Si/Ta(50)/Pt-Mn(20)/Co-Fe(2)/Ru(0.8)/Co-Fe(3)/MgO(1)/Co-Fe-B(2.5)/Ta(10)/Pt(5), where the numbers in parentheses are thicknesses in nanometers. The resistance-area product for this unpatterned film is $5.4 \Omega \cdot \mu\text{m}^2$ [17]. This stack is coated with a Ta layer for adhesion followed by Pt in order to maintain an electrically conducting surface for conductive atomic force microscopy (CAFM) measurements. To pattern the stack into nanodots, a SiN_x hard mask is first deposited and the hydrogen silsesquioxane photoresist is spin coated. Arrays

*sara@cmu.edu

of circular dots with nominal diameters of 20–80 nm are written using electron beam lithography with an FEI Sirion 600 scanning electron microscope operating at 30 kV. To minimize magnetostatic interactions, the distance between adjacent dots is 250 nm. These features are transferred to the stack by ion milling down to the MgO layer. The SiN_x layer is removed by CF_4 -based reactive ion etching in a Plasma Therm 790.

Figures 1(a) and 1(b) show schematics of the film stack before and after patterning. Figure 1(c) shows a scanning electron microscopy (SEM) image of arrays of the circular MTJ devices after patterning. The actual diameters of the dots described here in detail are 25, 41, 60, and 80 nm, all ± 2 nm, but the text refers to the nominal diameters 20, 40, 60, and 80 nm, respectively.

Prior to patterning the top Co-Fe-B layer into nanodots, magnetization curves are measured by alternating gradient magnetometry. In-plane measurements are used to determine switching field of the reference layer (see Fig. S1 within the Supplemental Material) [18] and out-of-plane measurements are used to estimate the saturation field of the free layer (see Fig. S2 within the Supplemental Material) [18].

B. Conductive atomic force microscopy

An RHK UHV350 conductive atomic force microscope with an R9 controller is used for transport measurements at room temperature. CAFM measurements used a commercial silicon-doped atomic force microscope tip (NanoAndmore USA) coated with a 5-nm Ta layer for adhesion followed by 200 nm Pt. Further details about these measurements have been reported previously [9,19,20].

Several types of measurements are conducted. Normal force measurements are conducted to check the topography of the patterned sample and to verify the pillar height of 14 nm. For CAFM magnetoresistance measurements, the tip is brought into contact with the top Pt layer of the Co-Fe-B dot. Most of the field-dependent measurements are made with the external field parallel to the axis of the antiferromagnetic Pt-Mn pinning layer. The fixed layer is initialized by applying an in-plane field of 0.4 T along the

pinning direction using a permanent magnet. After removing the permanent magnet, an electromagnet is used to generate a variable in-plane field of up to 500 G.

Measurements of the resistance as a function of magnetic field, $R(H)$, showed a small loop shift of 20–50 G, and the parallel (P) state is always favored for $H = 0$. The origin of the P state preference may arise from orange peel coupling [21–23], weak exchange coupling across MgO barriers of up to 1 nm [24], and/or local strains [25]. An external field is applied so that the local magnetic field H_{local} is close to zero, so that the data could be analyzed in terms of purely voltage- or current-driven effects. $R(V)$ measurements are recorded by sweeping the bias at a rate of 1.5 V/s while measuring the resistance. Positive bias corresponds to electrons flowing from the tip into the sample. Time traces, $R(t)$, of the resistance are measured with $H_{\text{local}} \approx 0$, at different currents or bias voltages. The data acquisition rate is 100 MHz and the acquisition time is a total of 26 ms at each bias. With a Red Pitaya interface for rapid data acquisition, the effective RC time constant for our system is found to be approximately 700 ns.

C. Atomistic magnetic simulations

Atomistic spin dynamics simulations [26] using the VAMPIRE software package [27] are carried out to investigate magnetization reversal in circular Co-Fe-B disks 20, 40, 60, and 80 nm in diameter and 2.5 nm in thickness. A detailed treatment including a polycrystalline oxide shell, with more realistic surface and interface effects, is planned for the future. Here we use a highly simplified model in order to understand whether the reversal is coherent rotation-like for the different sizes, and to determine the effect of a high-anisotropy cobalt ferrite-like shell on the average reversal field. In our model, Co-Fe-B is treated as an average magnetic material with a body-centered cubic lattice (lattice constant, $a = 2.86$ Å), an atomic spin moment of $1.6 \mu_B$, exchange $J_{ij} = 7.735 \times 10^{-21}$ J/link and cubic anisotropy $K = 4.68 \times 10^{-25}$ J/atom [28,29]. The oxide shell is also simplified by modeling using the same lattice that is used for Co-Fe-B but with an atomic spin moment of approximately $0.57 \mu_B$ corresponding to

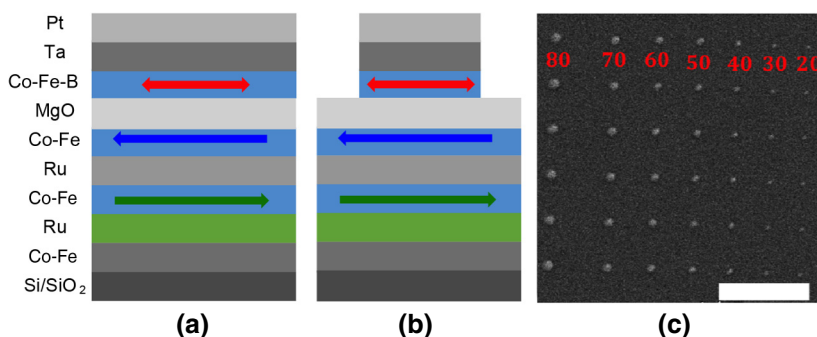


FIG. 1. The sample stack (a) before and (b) after patterning to the MgO layer, with thicknesses given in nanometers. (c) SEM micrograph of array of circular dots with different sizes. The size of the scale bar is $1 \mu\text{m}$, and the numbers correspond to the nominal dot diameter in nanometers.

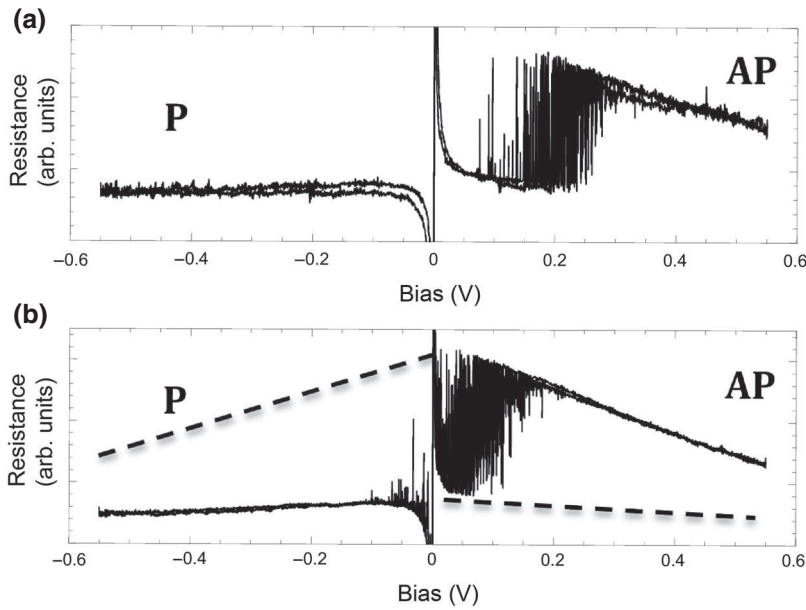


FIG. 2. Resistance as a function of voltage across the tunnel junction, for a 60-nm diameter dot, measured with a ramp rate of 0.5 V/s. (a) With an external field $H=0$ but a 14-Oe $R(H)$ loop shift due to the stray field. (b) After cancellation of the stray field. In the telegraphing region the resistance fluctuates rapidly between the parallel (P) and antiparallel (AP) resistance levels. The dashed lines are guides to the eye.

bulk M_s of 4.55×10^5 A/m and cubic anisotropy K of 2.9×10^5 J/m, matching the values of CoFe_2O_4 [30].

Simulated hysteresis loops are conducted at both room temperature and 0 K, including dipole-field effects using the macrocell approach [31,32]. The system is initialized in the [100] direction and a magnetic field is applied in the same direction and incrementally swept from a saturating positive field to a saturating negative field and back to the same starting positive field, at a rate of 0.05 T/ns and with critical Gilbert damping to give quasistatic hysteresis loops. Both the magnetization and spin configuration are recorded at each field increment.

III. RESULTS AND DISCUSSION

Figure 2 shows the resistance as a function of voltage without and with a correction for a small magnetic stray field. In both cases there is a region with telegraphing between the P and AP states. At large positive bias there is no telegraphing because the device is always in the AP state; similarly, at large negative bias it is always in the P state. Note that even with $H_{\text{local}} \approx 0$ the $R(V)$ loop is asymmetric. This is consistent with the asymmetry of STT reversal in a magnetic tunnel junction with deterministic switching [33].

Figure 3 shows how the resistance of the 60-nm dot of Fig. 2 fluctuates over time for different currents, all with $H_{\text{local}}=0$. At $-18 \mu\text{A}$ it is almost always in the P state, while at $+235 \mu\text{A}$ it spends most of the time in the AP state. Here positive current indicates that electrons are flowing from the tip through the dot to the reference layer. Raising the current increases the average retention time

in the AP state, consistent with STT-assisted reversal. In some of the time traces there appear to be partial switching events. In larger elliptical spin-valve devices, evidence has been seen for intermediate states, based on characteristic resistance levels midway between the P and AP values [34]. However, in our samples the magnitude of the intermediate resistance varies randomly, and the intermediate state is never stable longer than a microsecond. Most likely the nanodot switches back and forth within this period, and we are limited by the RC time constant of the electronics. For our analysis, we identified a threshold beyond which the dot is considered to be in either a P or AP state, and then treated partial switches beyond the thresholds as full switches.

The data of Fig. 3 are analyzed to determine the retention times τ_P and τ_{AP} between switching events. For a given trace, a histogram is made of the number of times the resistance is stable in the P state for a time τ_{Pi} over 2.6 ms. The characteristic retention time τ_P is found from fitting this data to an exponential function, excluding the shortest times where the count rate is distorted by the time constant of the capture electronics. Similar analysis is done for the AP state. These results, along with the average retention time $\bar{\tau} = [\tau_P^{-1} + \tau_{AP}^{-1}]^{-1}$, are shown in Figs. 4(a) and 4(b).

For comparison of dots of different diameters, we estimated the 50:50 point, defined as where the dot spends equal time in the P and AP states. For the 60-nm dot of Fig. 3 the estimated 50:50 point occurs near $100 \mu\text{A}$. The current density is roughly comparable for different dots at the 50:50 point, and typical of the critical current density for STT switching in stable MTJs. While many different dots of each size are studied, the detailed characterization focused on four dots in the same area, measured on the

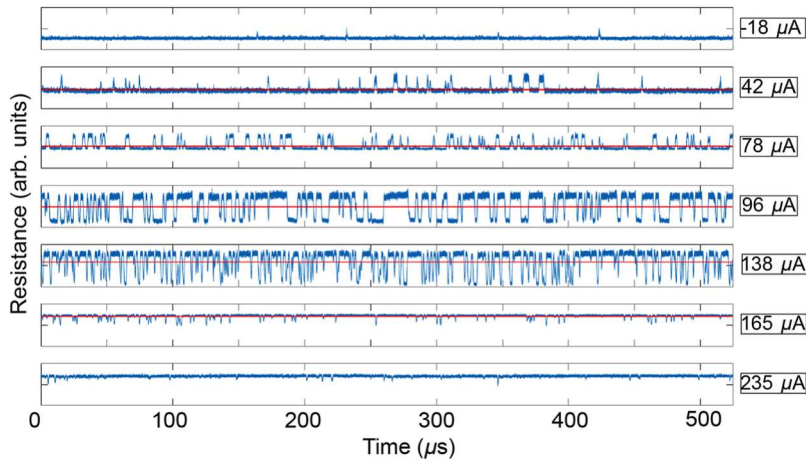


FIG. 3. Resistance as a function of time, for different tunnel currents at $H_{\text{local}} \approx 0$, offset for clarity. The blue lines show the resistance fluctuations, and the red lines indicate the average resistances over the entire 26-ms capture time, but a smaller time window is shown, so that the current-induced differences in the switching frequencies are clearer.

same day. Table I details the 50:50 point as a function of dot diameter.

Size-dependent differences in magnetic relaxation are quantified using the autocorrelation function (ACF) of the time-dependent resistance at the 50:50 point, defined by

$$\text{ACF} = \frac{\sum_{i=1}^{N-T} [R_i - \bar{R}][R_{i+T} - \bar{R}]}{\sum_{i=1}^N [R_i - \bar{R}]^2}. \quad (1)$$

Here the time traces are digitized and the summation is taken over lag times T . Figure 4(c) shows the autocorrelation functions for the different sizes. If a process is Markovian, the ACF will have an exponential decay with a characteristic relaxation time. This is observed for the larger sizes, but curvature is noticeable in the 20-nm data. The origin of the deviation is seen by comparing the distribution of retention times in the P and AP states. For the 20-nm dot τ_P and τ_{AP} differ by a factor of 3, even though the dot spends equal times in both states. Figure 4(b) shows that the average retention time as a function of current is sharply peaked. The difference between the P and AP

retention times could also indicate that the local field is not precisely canceled. While the exact values are sensitive to incompletely compensated stray fields (1–2 Oe), the trend in the size dependence is clear: the smaller dots switch *less* frequently.

In a superparamagnetic nanoparticle, smaller sizes are expected to fluctuate more rapidly. Here the dots are destabilized with the aid of STT, but at the 50:50 point the differences in retention time between switching events are associated with thermal fluctuations that can lead to spontaneous switching. A possible origin of the enhanced stability for small Co-Fe-B dots is exchange bias between a thin oxide layer on the sidewalls and the metallic dot interior. If so, then the current densities of Table I would be underestimated, particularly for the smaller dot sizes. In Fe or Co nanoparticles [35–38] and the sidewalls of Co-Fe-B-based magnetic tunnel junctions [38], there is a thin layer of oxide, which is polycrystalline and has randomly oriented grains. Unfortunately, the shell thickness could not be determined directly for these nanodots, but in similar structures the thickness is estimated to be

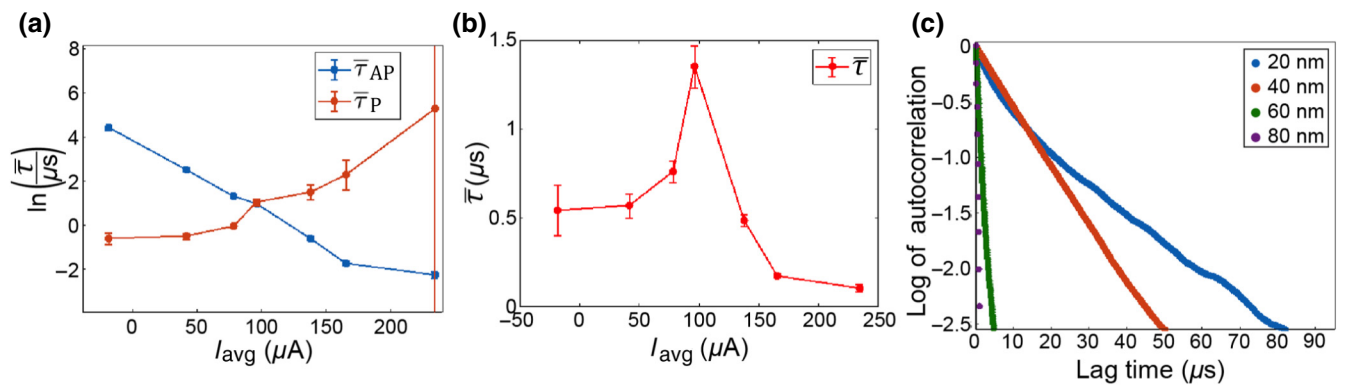


FIG. 4. (a) Average retention times in the P and AP states as a function of tunnel current, for the 60-nm dot of Fig. 3. Here the relaxation times are normalized to $1 \mu\text{s}$. (b) Average retention time τ vs current for the same dot. (c) Normalized autocorrelation function for the different sizes at the approximate 50:50 point.

TABLE I. Size-dependent properties of the 50:50 point.

Nominal size (nm)	Actual size (nm)	% time in P state	Average J ($\times 10^6$ A/cm 2)	Average τ (μ s)
20	25 ± 2	50.3	5.35	13.7 ± 3.5
40	41 ± 2	48.7	5.74	19.8 ± 3.3
60	60 ± 2	52.0	3.41	1.35 ± 0.20
80	80 ± 2	47.5	6.35	0.49 ± 0.03

approximately 2 nm [39], and for oxidized Fe nanoparticles approximately 4 nm [40]. Just as ferromagnetic cobalt ferrite has a much larger anisotropy than Co-Fe, the surface oxide here, Co-Fe-B-O $_x$, is likely to be ferrimagnetic and of higher anisotropy than Co-Fe-B. Surface oxidation has previously been reported to increase anisotropy and reduce the switching field distribution for Co-Fe-B MTJs [41].

To quantify exchange-bias effects, samples are typically cooled in large (5 T) magnetic fields, and the shift in the hysteresis loop is measured. Unfortunately, such experiments are not feasible with our measurement technique, but training effects are evident even at 300 K with modest magnetic fields (± 500 G). Here training is achieved via multiple measurements of asymmetric hysteresis loops, as seen in Fig. 5. With a symmetric loop between ± 500 G, this 40-nm pillar has switching fields at roughly -20 and $+80$ G. After positive training (20 loops with 5 s per loop) the coercivity is reduced to approximately 10 G and switching occurs near $+80$ G. The same device has low coercivity and switches near -20 G after negative training. Telegraphing is observed within 10 G of the switching fields, but in the untrained case these fields are well separated and the dot did not telegraph at $H = 0$. These training effects relaxed within 1–5 min.

Some training effects are seen in individual dots of all sizes, but the effects are much more pronounced for 40- and

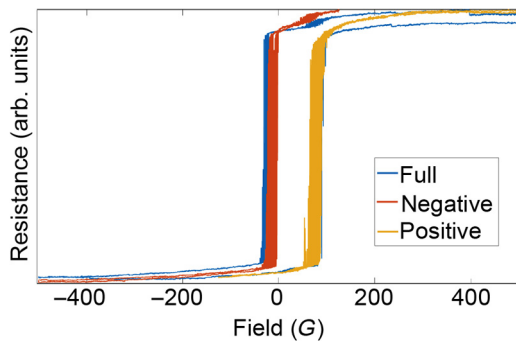


FIG. 5. 40-nm pillar resistance as a function of magnetic field, measured at 100-mV bias. Before training (blue), the full loop is symmetric, with switches near -20 and $+80$ G. After 10 loops of positive training (-125 to $+500$ G), the asymmetric loop shows all the switching clustered around $+80$ G (yellow). After six loops of negative training (-500 to $+125$ G), all the switching is clustered around -20 G (red).

20-nm diameters. (See Fig. S3 within the Supplemental Material [18].) In the smaller dots there are often clear and repeatable jumps in the resistance, such as that in the upper branch of Fig. 5, due to depinning. The smaller dots have proportionately more switching at higher fields, indicating a greater fraction of pinned magnetization, and consistent with slower telegraphing. Two-level telegraphing is observed for all sizes, indicating uniaxial behavior.

In nanoparticles with exchange bias, the surface oxide is polycrystalline, and there are variations in the oxide grain size and orientation. Sidewall oxidation in the nanodots is expected to be similar. To test this, $R(H)$ loops are measured after rotating the sample so that the applied magnetic field is perpendicular to the Pt-Mn pinning axis of the fixed layer. (See Fig. S4 within the Supplemental Material [18].) The 60- and 80-nm devices show typical hard-axis behavior. Some of the smaller dots behave similarly, but other cases have more of an easy-axis loop shape. Strong exchange bias to oxide grains could therefore alter the easy axis of the dot, creating a more complex energy landscape for switching, and leading to variations for different dots.

Atomistic spin dynamics simulations are used to understand the effects of surface oxide on dots of different diameters. The accessible timescale of these simulations is much shorter than that of the experimental measurements, so that the magnetization does not follow a Langevin function. However, the relative coercivities should correlate with the transition rate between the P and AP states. For pristine (unoxidized) dots at 0 K, the coercivities are equal to the anisotropy field, and therefore independent of size, as shown in Fig. 6(a). At 300 K the coercivity of all the dots without edge oxidation in Fig. 6(b) is significantly reduced due to thermal spin fluctuations and a systematic trend is also seen with a larger reduction for the smaller dot sizes. The 20-nm dot shows an asymmetric hysteresis loop due to random thermal fluctuations during the simulation.

For the oxidized dots, the edge oxidation is assumed to be quasipassivating, and therefore the same thickness for all sizes. For the simulations the maximum plausible shell thickness, 4 nm, and the maximum anisotropy, that of CoFe $_2$ O $_4$, are assumed, and the shell is treated as a single grain, although in reality the oxide is likely to be polycrystalline. Figure 6(c) shows the simulated 0 K hysteresis loops. Now H_c is largest for the 20-nm dot, since it has the largest proportion of cobalt ferrite. For the dots with edge oxidation at 300 K in Fig. 6(d) the coercivity

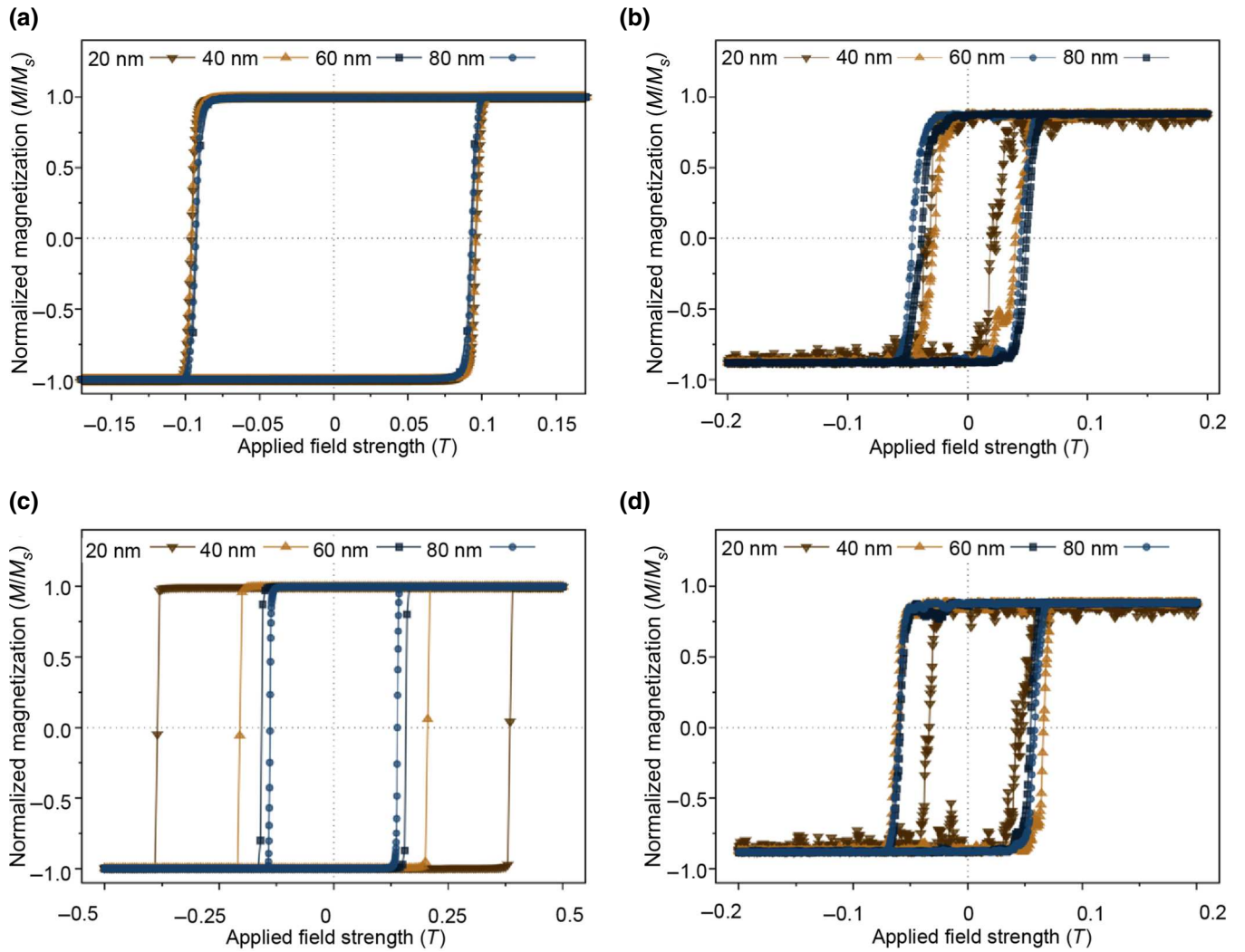


FIG. 6. Simulated hysteresis loops for different dot diameters, where (a) dots are unoxidized, $T = 0$ K, (b) dots are unoxidized, $T = 300$ K, (c) dots have a 4-nm thick cobalt ferrite shell, $T = 0$ K, and (d) dots have a cobalt ferrite shell, $T = 300$ K.

no longer shows a systematic size variation due either to thermal fluctuations or to different oxide shell thicknesses.

For all but the smallest dot size the coercivity is larger than in the case of no edge oxidation, demonstrating the increase in thermal stability. For the 20-nm diameter dots the effect of edge oxidation at elevated temperatures is less clear due to large thermal fluctuations but suggests a small increase in coercivity due to the shell. The simulations may overestimate the magnetocrystalline anisotropy contribution from the oxide shell, but they omit the effect of pinning sites, which arise from the polycrystalline nature of the oxide, and are sometimes detected through the experimental jumps in magnetoresistance. In the simulations the oxide shell completely reverses during hysteresis due to its ferrimagnetic nature, while in reality the shell is likely to include an irreversible component that could significantly enhance the thermal stability of the smallest dots.

Overall, the simulated coercivities of the unoxidized dots are inconsistent with the relative stabilities found experimentally, where the smaller dots are less thermally stable. The reversal mechanism is always coherent for in-plane dots, while thinner dots with an out-of-plane magnetization show a size-dependent transition from coherent to incoherent reversal [28].

Figures 6(b) and show hysteresis loops at 300 K for dots with and without a 4-nm oxide shell. Figure 7 shows images of the spin configuration within the 20 and 60 dots, taken at fields near the coercivity. The main effect of the shell is to increase the field where reversal occurs. While there are local fluctuations the magnetization is predominantly in-plane during reversal, for all of the sizes studied, both with and without an oxide shell. At finite temperature, fluctuations occur within the dot, especially near the edges, and may lead to reversal. Exchange coupling between the low-K interior and high-K shell suppresses the likelihood

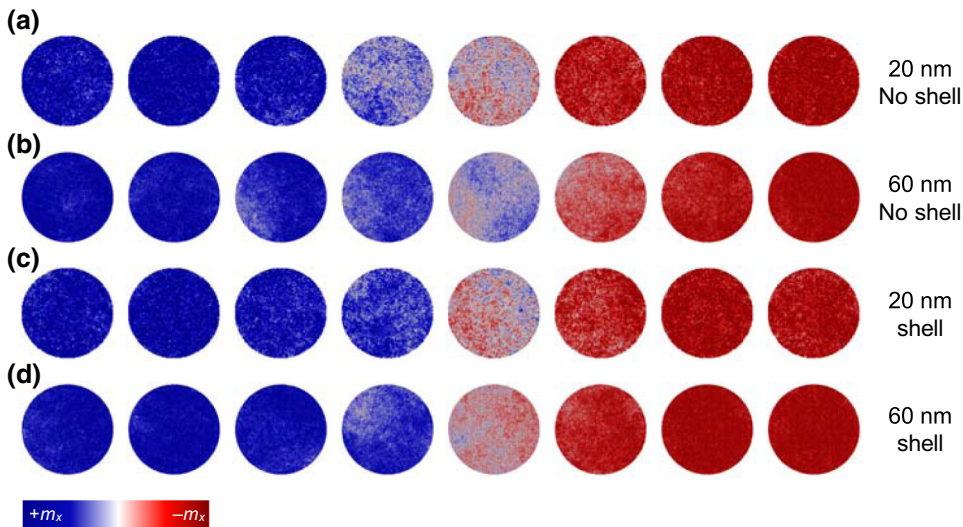


FIG. 7. In-plane magnetization components during reversal, at 300 K. (a) 20-nm Co-Fe-B dot with no shell. (b) 60-nm dot with no shell. (c) 20-nm dot including a 4-nm-thick CoFe_2O_4 shell. (d) 60-nm dot including a 4-nm shell.

that an edge fluctuation leads to reversal. Inhomogeneity in K in different parts of the shell, which would be expected for real nanodots, would also increase the time between switching from P to AP states, and vice versa.

Since we do not observe a repeatable, metastable intermediate resistance, the reversal from P to AP is still fast with respect to our measurement time.

IV. CONCLUSIONS

We show that spin-transfer torque can drive individual magnetic nanodots into a superparamagnetic state. The physical origin is similar to that for deterministic STT switching of thermally stable nanomagnets, except that instead of hysteresis, the current causes telegraph noise in the metastable region. The current density determines the equilibrium or time-averaged magnetization of the superparamagnet, but not the retention time in a particular state.

The magnetization dynamics are measured over a time window extending from hundreds of nanoseconds to tens of milliseconds, a shift to shorter times compared with previous studies of random telegraph noise [7,15,42–44]. In a pristine state, smaller superparamagnetic particles will switch more frequently, but this is not observed experimentally for these nanodots. The deviation is due to exchange bias due to a thin oxide layer at the edge of the nanodots. The time-averaged magnetization for a particular dot diameter is determined by the current density through the Co-Fe-B center. The relative stability of the dot, as reflected by the average retention time between stochastic switches, is dominated by the exchange coupling between the Co-Fe-B center and the high-anisotropy oxide grains at the edges.

We show that exchange-bias measurements can be made on single nanomagnets, analogous to core-shell nanoparticles. As with magnetization measurements on ensembles

of nanoparticles, single nanomagnet magnetoresistance confirms that exchange bias enhances overall stability with respect to thermal fluctuations. In addition, these measurements reveal that nanomagnets are susceptible to training effects even at high temperature and low magnetic field. The ability to measure on a short timescale is key; just as the coercivity of magnetic recording media is increased by a short measurement time, so exchange-bias effects are more pronounced when probed on a microsecond timescale.

The findings are also relevant for devices with layered nanomagnets such as MRAM and STOs. As such devices get smaller and are more susceptible to thermal fluctuations, variations in device-to-device performance increase. This is often attributed to differences associated with lithographic processing. Our results suggest that differences in the sidewall passivation could also contribute. Previous workers have shown that monodomain dots have a variable incubation time prior to rapid (approximately 1.5 ns) switching [45,46], and that the distribution of incubation times is greater for smaller sizes. The delay is attributed to the time needed to climb the energy barrier. A small amount of edge oxidation, which increases the barrier height, could also delay reversal. The phase noise of an STO has been modeled using a macrospin for the magnetic moment of the nanodot, together with a Néel–Brown model for stochastic fluctuations [47]. Our simulations show that edge oxidation modifies the fluctuations by effectively pinning the spins near the interface. Since the actual edge oxidation can be inhomogeneous, this could be a source of phase noise and its device-to-device variation.

ACKNOWLEDGMENTS

S.A.M. acknowledges support from US NSF Grants Nos. DMR-1407435 and No. ECCS-1709845. The simulations were undertaken on the VIKING Cluster, which

is a high-performance computer facility provided by the University of York. R.F.L.E. is grateful for computational support from the University of York High Performance Computing service, VIKING and the Research Computing team. We thank M. Bapna for patterning the sample.

-
- [1] L. Néel, Sur les effets des interactions entre les domaines élémentaires ferromagnétiques: Bascule et reptation, *J. Phys. Radium* **20**, 215 (1959); L. Néel, Influence des fluctuations thermiques à l'aimantation des particules ferromagnétiques, *C. R. Acad. Sci.* **228**, 664 (1949).
- [2] W. F. Brown, Jr., Thermal fluctuations of a single-domain particle, *Phys. Rev.* **130**, 1677 (1963).
- [3] C. P. Bean and J. D. Livingston, Superparamagnetism, *J. Appl. Phys.* **30**, S120 (1959).
- [4] W. T. Coffey and Y. P. Kalmykov, Thermal fluctuations of magnetic nanoparticles: Fifty years after Brown, *J. Appl. Phys.* **112**, 121301 (2012).
- [5] Q. A. Pankhurst, J. Connolly, S. K. Jones, and J. Dobson, Application of magnetic nanoparticles in biomedicine, *J. Phys. D* **36**, R167 (2003).
- [6] K. M. Krishnan, Biomedical nanomagnetism: A spin through possibilities in imaging, diagnostics, and therapy, *IEEE Trans. Magn.* **46**, 2523 (2010).
- [7] J. Torrejon, M. Riou, F. A. Araujo, S. Tsunegi, G. Khalsa, D. Querlioz, P. Bortolotti, V. Cros, K. Yakushiji, A. Fukushima, H. Kubota, S. Yuasa, M. D. Stiles, and J. Grollier, Neuromorphic computing with nanoscale spintronic oscillators, *Nature* **547**, 428 (2017).
- [8] A. Z. Pervaiz, L. A. Ghantasala, K. Y. Camsari, and S. Datta, Hardware emulation of stochastic p-bits for invertible logic, *Sci. Rep.* **7**, 10994 (2017).
- [9] M. Bapna and S. A. Majetich, Current control of time-averaged magnetization in superparamagnetic tunnel junctions, *Appl. Phys. Lett.* **111**, 243107 (2017).
- [10] W. A. Borders, A. Z. Pervaiz, S. Fukami, K. Y. Camsari, H. Ohna, and S. Datta, Integer factorization using stochastic magnetic tunnel junctions, *Nature* **573**, 390 (2019).
- [11] H. Sato, M. Yamanouchi, K. Miura, S. Ikeda, H. D. Gan, K. Mizunuma, R. Koizumi, F. Matsukura, and H. Ohno, Junction size effect on switching current and thermal stability in CoFeB/MgO perpendicular magnetic tunnel junctions, *Appl. Phys. Lett.* **99**, 042501 (2011).
- [12] H. Sato, E. C. I. Enobio, M. Yamanouchi, S. Ikeda, S. Fukami, S. Kanai, F. Matsukura, and H. Ohno, Properties of magnetic tunnel junctions with a MgO/CoFeB/Ta/CoFeB/MgO recording structure down to junction diameter of 11 nm, *Appl. Phys. Lett.* **105**, 062403 (2014).
- [13] J. J. Nowak, R. P. Robertazzi, J. Z. Sun, G. Hu, J. H. Park, J. H. Lee, A. J. Annunziata, G. P. Lauer, R. Kothandaraman, E. J. O'Sullivan, P. L. Trouilloud, Y. Kim, and D. C. Worledge, Dependence of voltage and size on write-error rates in spin-transfer torque magnetic random-access memory, *IEEE Magn. Lett.* **7**, 3102604 (2016).
- [14] M. Zahedinejad, A. A. Awad, P. Dürrenfeld, A. Houshang, Y. Yin, P. K. Muduli, and J. Åkerman, Current modulation of nanoconstriction spin Hall nano-oscillators, *IEEE Magn. Lett.* **8**, 3104804 (2017); A. A. Awad, P. Dürrenfeld, A. Houshang, M. Dvornik, E. Iacocca, R. K. Dumas, and J. Åkerman, Long-range mutual synchronization of spin Hall nano-oscillators, *Nat. Phys.* **13**, 292 (2017).
- [15] B. Parks, M. Bapna, J. Igbokwe, H. Almasi, W. Wang, and S. A. Majetich, Superparamagnetic perpendicular magnetic tunnel junctions for true random number generators, *AIP Adv.* **8**, 055903 (2018).
- [16] R. W. Dave, G. Steiner, J. M. Slaughter, J. J. Sun, B. Craigo, S. Pietambaram, K. Smith, G. Grynkewich, M. DeHerrera, J. Åkerman, and S. Tehrani, MgO-based tunnel junction material for high-speed toggle random access memory, *IEEE Trans. Magn.* **42**, 1935 (2006).
- [17] E. R. Evarts, L. Cao, D. S. Ricketts, N. D. Rizzo, J. A. Bain, and S. A. Majetich, Spin torque transfer switching of magnetic tunnel junctions using a conductive atomic force microscope tip, *Appl. Phys. Lett.* **95**, 132510 (2009).
- [18] See Supplemental Material at <http://link.aps.org/supplemental/10.1103/PhysRevApplied.13.014063> for magnetometry of the unpatterned film stack, additional results from training experiments, and magnetoresistance hysteresis loops taken with the applied field perpendicular to the pinning axis.
- [19] S. K. Piotrowski, M. Bapna, S. D. Oberdick, S. A. Majetich, M. Li, C. L. Chien, R. Ahmed, and R. H. Victora, Size and voltage dependence of effective anisotropy in Co₄₀Fe₄₀B₂₀ magnetic tunnel junctions, *Phys. Rev. B* **94**, 014404 (2016).
- [20] S. K. Piotrowski, M. F. Matty, and S. A. Majetich, Magnetic fluctuations in individual superparamagnetic particles, *IEEE Trans. Mag.* **50**, 2303704 (2014).
- [21] F. A. Shah, V. K. Sankar, P. Li, G. Csaba, E. Chen, and G. H. Bernstein, Extraordinary Hall effect based magnetic logic applications, *J. Appl. Phys.* **115**, 17B902 (2014).
- [22] J. Moritz, F. Garcia, J. C. Toussaint, B. Dieny, and J. P. Nozières, Orange peel coupling in multilayers with perpendicular anisotropy: Application to (Co/Pt)-based exchange-biased spin valves, *Europhys. Lett.* **65**, 123 (2004).
- [23] A. Guedes, M. J. Mendes, P. P. Freitas, and J. L. Martins, Study of synthetic ferrimagnet-synthetic antiferromagnet structures for magnetic sensor application, *J. Appl. Phys.* **99**, 08B703 (2006).
- [24] T. Katayama, S. Yuasa, J. Velez, M. Ye. Zhuravlev, S. S. Jaswal, and E. Y. Tsymlal, Interlayer exchange coupling in Fe/MgO/Fe magnetic tunnel junctions, *Appl. Phys. Lett.* **89**, 112503 (2006).
- [25] X. X. Jiang, Z. Li, Y. Zheng, C. Kaiser, Z. Diao, J. Fang, and Q. Leng, Modulation of interlayer exchange coupling via strain effect, *AIP Adv.* **5**, 097221 (2015).
- [26] R. F. L. Evans, W. J. Fan, P. Chureemart, T. A. Ostler, M. O. A. Ellis, and R. W. Chantrell, Atomistic spin model simulations of magnetic nanomaterials, *J. Phys. Condens. Matter* **26**, 10 (2014).
- [27] VAMPIRE software package v6.0 (Git hash b2e49c969ea59f4ee49056d56b2a3b0208b25ac8) available from <https://vampire.york.ac.uk/>.
- [28] A. Meo, P. Chureemart, S. Wang, R. Chepulskyy, D. Apalkov, R. W. Chantrell, and R. F. L. Evans, Thermally nucleated magnetic reversal in CoFeB/MgO nanodots, *Sci. Rep.* **7**, 16729 (2017).

- [29] H. Sato, P. Chureemart, F. Matsukura, R. W. Chantrell, H. Ohno, and R. F. L. Evans, Temperature-dependent properties of CoFeB/MgO thin films: Experiments versus simulations, *Phys. Rev. B* **98**, 214428 (2018).
- [30] F. Eskandari, S. B. Porter, M. Venkatesan, P. Kameli, K. Rode, and J. M. D. Coey, Magnetization and anisotropy of cobalt ferrite thin films, *Phys. Rev. Mater.* **1**, 074413 (2017).
- [31] G. J. Bowden, G. B. G. Stenning, and G. van der Laan, Inter and intra macro-cell model for point dipole–dipole energy calculations, *J. Phys. Condens. Matter* **28**, 6 (2016).
- [32] A. Meo, Ph. D. thesis, University of York, 2018.
- [33] S. Ikeda, K. Miura, H. Yamamoto, K. Mizunuma, H. D. Gan, M. Endo, S. Kanai, J. Hayakawa, F. Matsukura, and H. Ohno, A perpendicular-anisotropy CoFeB-MgO magnetic tunnel junction, *Nat. Mater.* **9**, 721 (2010).
- [34] D. B. Gopman, D. Bedau, S. Mangin, C. H. Lambert, J. A. Katine, E. E. Fullerton, and A. D. Kent, Asymmetric switching behavior in perpendicularly nanopillars due to the polarizer dipole field, *Appl. Phys. Lett.* **100**, 062404 (2012).
- [35] G. H. Wen, R. K. Zheng, K. K. Fung, and X. X. Zhang, Microstructural and magnetic properties of passivated Co nanoparticle films, *J. Magn. Magn. Mater.* **270**, 407 (2004).
- [36] W. H. Meiklejohn and C. P. Bean, New magnetic anisotropy, *Phys. Rev.* **105**, 904 (1956).
- [37] V. Skumryev, S. Stoyanov, Y. Zhang, G. Hadjipanayis, D. Givord, and J. Nogues, Beating the superparamagnetic limit with exchange bias, *Nature* **423**, 850 (2003).
- [38] D. Givord, V. Skumryev, and J. Nogues, Exchange coupling mechanism for magnetization reversal and thermal stability of Co nanoparticles embedded in a CoO matrix, *J. Magn. Magn. Mater.* **294**, 111 (2005).
- [39] L. Tryputen, K.-H. Tu, S. K. Piotrowski, M. Bapna, S. A. Majetich, C. Sun, P. Voyles, H. Almasi, W.-G. Wang, P. Vargas, J. Tresback, and C. A. Ross, Patterning of sub-50 nm perpendicular CoFeB/MgO-based magnetic tunnel junctions, *Nanotechnology* **27**, 185302 (2016).
- [40] Y. S. Kwok, X. X. Zhang, B. Qin, and K. K. Fung, High resolution transmission electron microscopy study of epitaxial oxide shell on nanoparticles of iron, *Appl. Phys. Lett.* **77**, 3971 (2000).
- [41] T. Takenaga, T. Kuroiwa, J. Tsuchimoto, R. Matsuda, S. Ueno, H. Takada, Y. Abe, and Y. Tokuda, Suppression of switching-field variation by surface oxidation depending on the shape of the CoFeB layer, *IEEE Trans. Mag.* **43**, 2352 (2007).
- [42] Y. Kim, H. Song, D. Kim, T. Lee, and H. Jeong, Noise characteristics of charge tunneling via localized states in metal-molecule-metal junctions, *ACS Nano* **4**, 4426 (2010).
- [43] R. Soni, P. Meuffels, A. Petraru, M. Weides, C. Kügeler, R. Waser, and H. Kohlstedt, Probing Cu doped Ge_{0.3}Se_{0.7} based resistance switching memory devices with random telegraph noise, *J. Appl. Phys.* **107**, 024517 (2010).
- [44] N. Clement, K. Nishiguchi, A. Fujiwara, and D. Vuillaume, One-by-one trap activation in silicon nanowire transistors, *Nat. Commun.* **1**, 92 (2010).
- [45] C. Hahn, G. Wolf, B. Kardasz, S. Watts, M. Pinarbasi, and A. D. Kent, Time-resolved studies of the spin-transfer reversal mechanism in perpendicularly magnetized magnetic tunnel junctions, *Phys. Rev. B* **94**, 214432 (2016).
- [46] F. Iga, Y. Yoshida, S. Ikeda, T. Hanyu, and H. Ohno, Time-resolved switching characteristic in magnetic tunnel junctions with spin transfer torque write scheme, *Jap. J. Appl. Phys.* **51**, 02BM02 (2012).
- [47] T. J. Silva and M. W. Keller, Theory of thermally induced phase noise in spin torque oscillators for a high-symmetry case, *IEEE Trans. Mag.* **46**, 3555 (2010).